Astronomy & Astrophysics manuscript no. 18223˙astroph
October 27, 2015
© ESO 2015

arXiv:1510.07063v1 [astro-ph.GA] 9 Oct 2015

Filament Fragmentation in High-Mass Star Formation⋆.

H. Beuther[1], S.E. Ragan[2], K. Johnston[2], Th. Henning[1], A. Hacar[3], and J.T. Kainulainen[1]

[1] Max Planck Institute for Astronomy, Königstuhl 17, 69117 Heidelberg, Germany, e-mail: name@mpia.de
[2] University of Leeds, Leeds, LS2 9JT, UK
[3] University of Vienna, Türkenschanzstr. 17, A-1180 Vienna, Austria

Version of October 27, 2015

ABSTRACT

Context. Filamentary structures in the interstellar medium are crucial ingredients in the star formation process. They fragment to form individual star-forming cores, and at the same time they may also funnel gas toward the central gas cores providing an additional gas reservoir.
Aims. We want to resolve the length-scales for filament formation and fragmentation (resolution ≤0.1 pc), in particular the Jeans length and cylinder fragmentation scale.
Methods. We have observed the prototypical high-mass star-forming filament IRDC 18223 with the Plateau de Bure Interferometer (PdBI) in the 3.2 mm continuum and N_2H^+(1–0) line emission in a ten field mosaic at a spatial resolution of ∼ 4″ (∼14000 AU).
Results. The dust continuum emission resolves the filament into a chain of at least 12 relatively regularly spaced cores. The mean separation between cores is ∼0.40(±0.18) pc. While this is approximately consistent with the fragmentation of an infinite, isothermal, gravitationally bound gas cylinder, a high mass-to-length ratio of $M/l \approx 1000\,M_\odot\,pc^{-1}$ requires additional turbulent and/or magnetic support against radial collapse of the filament. The $N_2H^+(1-0)$ data reveal a velocity gradient perpendicular to the main filament. Although rotation of the filament cannot be excluded, the data are also consistent with the main filament being comprised of several velocity-coherent sub-filaments. Furthermore, this velocity gradient perpendicular to the filament resembles recent results toward Serpens south that are interpreted as signatures of filament formation within magnetized and turbulent sheet-like structures. Lower-density gas tracers ([CI] and $C^{18}O$) reveal a similar red/blueshifted velocity structure on scales around 60″ east and west of the IRDC 18223 filament. This may tentatively be interpreted as a signature of the large-scale cloud and the smaller-scale filament being kinematically coupled. We do not identify a velocity gradient along the axis of the filament. This may either be due to no significant gas flows along the filamentary axis, but it may partly also be caused by a low inclination angle of the filament with respect to the plane of the sky that could minimize such signature.
Conclusions. The IRDC 18223 3.2 mm continuum data are consistent with thermal fragmentation of a gravitationally bound and compressible gas cylinder. However, the large mass-to-length ratio requires additional support – likely turbulence and/or magnetic fields – against collapse. The N_2H^+ spectral line data indicate a kinematic origin of the filament, but we cannot conclusively differentiate whether it has formed out of (pre-existing) velocity-coherent sub-filaments and/or whether magnetized converging gas flows, a larger-scale collapsing cloud or even rotation played a significant role during filament formation.

Key words. Stars: formation – Stars: early-type – Stars: individual: IRDC 18223 – Stars: massive – ISM: clouds – ISM: structure

1. Introduction

The existence of filaments in the interstellar medium has been known for a long time. Especially the arrival of the Herschel observatory has strongly increased the interest in filamentary structures, in particular as filaments are a main evolutionary stage during the formation of dense cores and stars (André et al. 2010; Henning et al. 2010; Men'shchikov et al. 2010; Arzoumanian et al. 2011; André et al. 2014). During star formation, filaments can fragment and form the seeds of the star-forming cores. Furthermore, gas can be funneled along the filaments and feed the star-forming regions (e.g., Schneider et al. 2010; Kirk et al. 2013; Myers 2013; Tackenberg et al. 2014). This is especially important for high-mass star formation because massive stars are likely fed from the larger-scale environment (e.g., Smith et al. 2009). Several filament studies have revealed filament parameters like their density structure, stability criteria, fragmentation length, characteristic width or kinematic properties (e.g., Johnstone et al. 2003; Jackson et al. 2010; Schneider et al. 2010; Henning et al. 2010; Beuther et al. 2011; Hacar et al. 2013; Hill et al. 2012; Kainulainen et al. 2013; Henshaw et al. 2014; Kainulainen et al. 2015). While large-scale low-mass star-forming regions have recently studied at high spatial resolution with CARMA (e.g., Fernández-López et al. 2014; Lee et al. 2014), many previous studies in the high-mass regime discussed spatial structures (on the order of 0.2 pc) based largely on single-dish measurements. Prominent exceptions are the infrared dark cloud investigated by Battersby et al. (2014), the hierarchical accretion study by Galván-Madrid et al. (2010) or the recent ALMA studies by, e.g., Peretto et al. (2013) or Zhang et al. (2015). The obvious goal is to investigate such filamentary structures at small spatial scales to study the physical properties of filaments on the scales of core and star formation on the order of 10000 AU. One recent high-resolution study of a massive filament has been performed by Henshaw et al. (2014) who do not find large velocity gradients across the filament but rather

⋆ Based on observations carried out with the IRAM Plateau de Bure Interferometer. IRAM is supported by INSU/CNRS (France), MPG (Germany) and IGN (Spain). The data are available in electronic form at the CDS via anonymous ftp to cdsarc.u-strasbg.fr (130.79.128.5) or via http://cdsweb.u-strasbg.fr/cgi-bin/qcat?J/A+A/

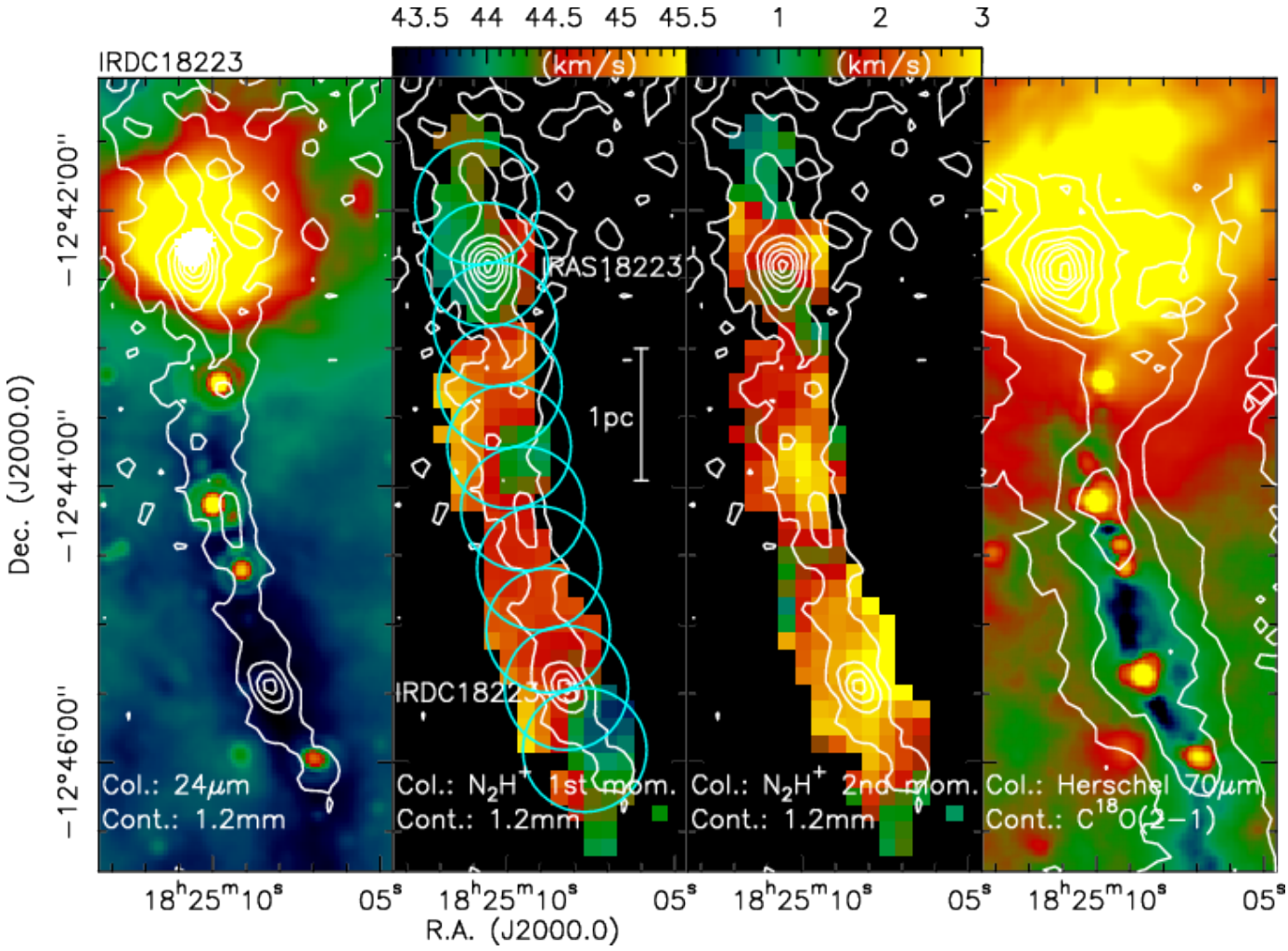

Fig. 1. The filamentary cloud IRDC 18223: The left panel presents the Spitzer 24 μm image in color (Beuther & Steinacker 2007), and the MAMBO 1.2 mm continuum map in contours (Beuther et al. 2002) with levels from 5 to 95% of the peak emission of 753 mJy beam^{-1} (in 10% steps). The 2nd and 3rd panels present the Nobeyama 45 m N_2H^+(1–0) 1st and 2nd moment maps, respectively (Tackenberg et al. 2014). The right panel shows the Herschel 70 μm observations (in color) and in contours the IRAM 30 m $C^{18}O$(2–1) data integrated from 40 to 49 km s^{-1}. The contours are from 5 to 95% of the peak emission of 18.6 K km s^{-1} (in 10% steps). Additionally, the middle panel shows the two main sources (the HMPO IRAS18223-1243 in the north and IRDC18223-3 in the south), a scale bar, as well as the positions of the 10 observed mosaic fields.

resolve it into velocity-coherent sub-structures, similar to the results of Hacar et al. (2013) for a low-mass filament in Taurus[1].

With the ultimate goal to understand high-mass star formation in filaments forming out of the larger-scale cloud, here we study the ~4 pc long infrared-dark filament associated with the High-Mass Protostellar Object (HMPO) IRAS 18223-1243 (Sridharan et al. 2002; Beuther et al. 2002). This region is part of a very long (>50 pc) filament previously investigated on larger scales by Kainulainen et al. (2011), Tackenberg et al. (2013), Ragan et al. (2014), and Zucker et al. (2015). The region is a well studied high-mass star formation complex at a distance of ~3.5 kpc encompassing various evolutionary stages from very young protostars embedded in an infrared dark cloud (IRDC) to forming HMPOs (e.g., Sridharan et al. 2002; Garay et al. 2004; Beuther et al. 2002, 2005; Beuther & Steinacker 2007; Beuther et al. 2010; Fallscheer et al. 2009). Based on Spitzer, Herschel and mm single-dish data, the mass and luminosity distribution of the filament is known in detail (e.g., Beuther et al. 2010; Ragan et al. 2012), and we now aim to shift the focus to the smaller scale dust and gas kinematic properties to set these into context with the larger-scale dust and gas filament.

For the region of this study, we have an extensive set of complementary data comprising – among others – the full Herschel far-infrared continuum data from 70 to 500 μm and additional ground based longer wavelength data (Beuther et al. 2010; Ragan et al. 2012), high-density N_2H^+(1–0) data from the Nobeyama 45 m telescope (Tackenberg et al. 2014), as well as [CII], [CI] and CO observations from SOFIA, APEX and the IRAM 30m telescope (Beuther et al. 2014). Figure 1 presents a compilation of different continuum and spectral line data of this region. However, while all these observations address the large-scale structure of the gas on scales of ~0.3 pc, no data existed so far that can investigate the fragmentation properties and kinematics of the region on scales comparable to the Jeans

[1] While Hacar et al. (2013) required filaments to be connected within sonic velocity separation, Henshaw et al. (2014) were less restrictive and allowed connected filaments based on the measured FWHM.

length. For example, average densities of high-mass star-forming regions around 10^5 cm^{-3} at low temperatures of 15 K result in typical Jeans fragmentation scales of around 10000 AU. These latter scales are now resolved with our new Plateau de Bure Interferometer 3 mm line and continuum data.

The main scientific questions to be addressed are: What is the relevant fragmentation scale of the filament itself? Is it consistent with Jeans fragmentation, isothermal gaseous cylinders or even more complex structures? What are the kinematic properties of the gas? Does it show velocity gradients along the filament indicative of global collapse (e.g., Tackenberg et al. 2014) or rather velocity coherent sub-filamentary structures (e.g., Hacar et al. 2013; Henshaw et al. 2014)? What are the virial parameters of the gas cores? What is the mass-per-unit length of the filament?

2. Observations

The IRDC 18223 filament was observed during a series of 8 tracks between June 2013 and April 2014 in the D- (with 5 antennas) and C-array (with 6 antennas) configurations of the Plateau de Bure Interferometer (PdBI). The projected baselines ranged between 15 and 175 m. While the absolute reference position was R.A. (J2000.0) 18h25m09.533s and Dec. (J2000.0) $-12^o43'55.90''$, ten mosaic pointings were required to cover the length of the filament (Fig. 1). The adopted velocity of rest $v_{\rm lsr}$ of the system is 45.3 km s^{-1}. Bandpass calibration was conducted with either of 3C279, 2200+420, 1633+382 or 3C345. The absolute flux calibration was performed with MWC349 and is estimated to be correct to within ∼15%. Phase and amplitude calibration was conducted with regular observations of the quasars 1730-130 and 1741-038. The spectral coverage of the wide-band receiver and correlator unit ranged from 91.53 to 95.14 GHz. Almost the whole bandpass was used to extract the 3.2 mm continuum emission (a small band around the $N_2H^+(1-0)$ was excluded). The narrow-band correlator units focused mainly on the $N_2H^+(1-0)$ and ^{13}CS(2–1) lines. The nominal channel separation was 0.039 MHz, and we smoothed the data to 0.2 km s^{-1} spectral resolution for our final data-cubes. While the $N_2H^+(1-0)$ emission was easily detected throughout the whole filament and will be discussed in detail in this paper, ^{13}CS(2–1) was only detected toward the strong northern IRAS source and will not be discussed any further. During the imaging process, we experimented with different weighting schemes between natural and uniform weighting to optimize the spatial resolution as well as signal-to-noise ratio. For the continuum emission we present both data with resulting synthesized beams of $5.6'' \times 3.27''$ (PA -6^o) and $4.37'' \times 2.84''$ (PA $+187^o$), respectively. For the $N_2H^+(1-0)$ data, we discuss the results based on the naturally weighted data with a synthesized beam of $5.77'' \times 3.39''$ (PA -6^o). The 1σ rms values are 0.13 mJy beam^{-1} for the continuum and 9 mJy beam^{-1} measured in a line-free channel of the $N_2H^+(1-0)$ emission.

Although Fig. 1 presents single-dish $N_2H^+(1-0)$ data from the Nobeyama 45 m telescope, neither the spectral resolution nor the sensitivity of these data is sufficient for merging with the new interferometer data. Therefore, we refrain from doing that.

3. Results

The IRDC 18223 represents a beautiful example of an infrared dark filament within a larger-scale filamentary structure covering more than 50 pc in linear extent (Kainulainen et al. 2011; Tackenberg et al. 2013; Ragan et al. 2014). In the following we will analyze in detail the dense gas and dust properties of this filament from a fragmentation and a kinematic point of view.

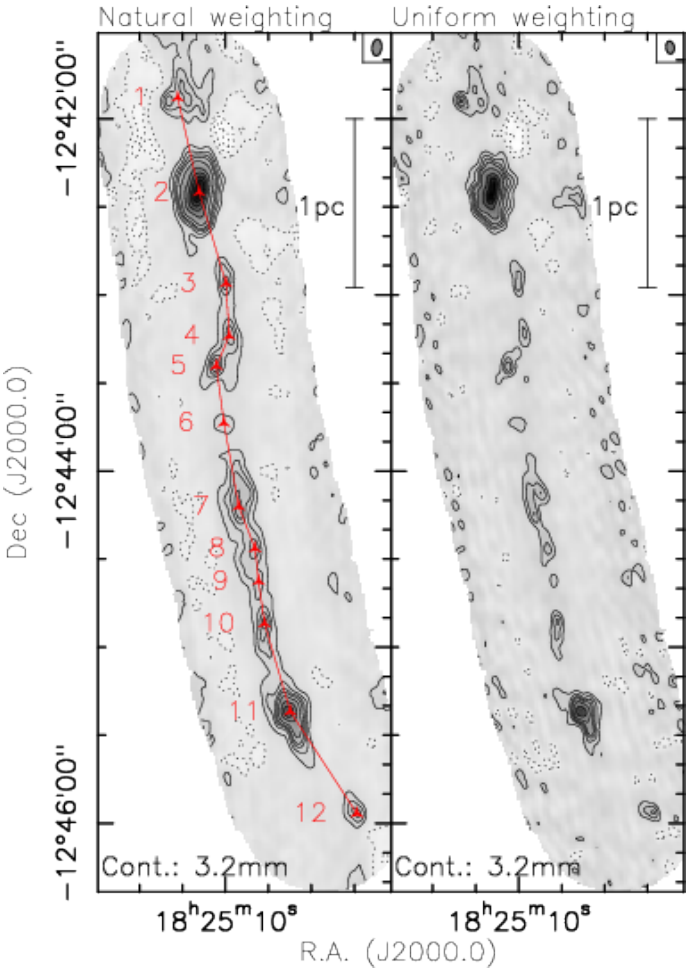

Fig. 2. 3.2 mm continuum images of the IRDC 18223 filament. The left panel is imaged with natural weighting and a resulting synthesized beam of $5.6'' \times 3.27''$ with a position angle of -6^o whereas the right image is conduced with uniform weight and a synthesized beam of $4.37'' \times 2.84''$ with a position angle of 187^o. The contour levels in both images start at the 3σ level of 0.39 mJy beam^{-1}, continuing in 3σ steps until 1.56 mJy beam^{-1} (the same are shown as dotted lines for negative features). Then they continue from 2.34 mJy beam^{-1} in 1.56 mJy beam^{-1} steps. The red markers and line in the left panel outline the main continuum peak positions and guide the eye for the filament structure. The synthesized beams and scale bars are shown in both panels at the top-right.

3.1. The filament in the 3.2 mm continuum emission

Figure 2 presents the 3.2 mm continuum data imaged with natural and uniform weighting. While the uniform weighting reveals more small-scale detail, the naturally-weighted imaged recovers more of the extended filamentary structure. Considering our spatial resolution limit of $4.37'' \times 2.84''$ that corresponds at the given distance of 3.5 kpc to a linear resolution element of ∼ 13000 AU, we cover scales of the filament between several pc down to ∼0.063 pc. With only a small large-scale velocity gradient along the filament (Sec. 3.2), IRDC 18223 may either have

barely any gas motions along the filament or have only a small inclination angle with respect to the plane of the sky. With an extent of ≥4 pc and an approximate width of on average less than 0.2 pc, its length-over-width ratio exceeds ∼20.

Fits to the spectral energy distributions of Spitzer and Herschel data toward individual cores in that region resulted in temperatures usually between 15 and 20 K for the cold component in this filament (Beuther & Steinacker 2007; Beuther et al. 2010; Ragan et al. 2012). For the following estimates we assume 15 K throughout the whole studied region. Assuming optically thin dust continuum emission at this temperature with a dust opacity $\kappa_{1.07\rm mm} \sim 0.8\,\rm cm^2\,g^{-1}$ at densities of $10^5\,\rm cm^{-3}$ (Ossenkopf & Henning 1994) and a gas-to-dust mass ratio of 150 (Draine 2011), the MAMBO 1.2 mm single-dish continuum data from Beuther et al. (2002) give an estimate of ∼4000 $\rm M_\odot$ total mass within the filament outlined in Figure 1[2]. Since bolometer arrays like MAMBO also filter large-scale emission, we can use the Herschel 500 μm data from Beuther et al. (2010)[3] to estimate the upper mass limit for the region. Integrating the Herschel 500 μm flux over the whole area shown in Fig. 2, we get a total flux of 187 Jy. With the same assumptions as above ($\kappa_{500\mu\rm m} \sim 3.9\,\rm cm^2\,g^{-1}$ at densities of $10^5\,\rm cm^{-3}$, Ossenkopf & Henning 1994), this results in a total gas mass in this area of ∼7673 $\rm M_\odot$, close to twice as much as measured by the MAMBO 1.2 mm data. Hence, the derived masses between 4000 and 7673 $\rm M_\odot$ bracket the overall mass of this star-forming large-scale filament. For comparison, the total 3.2 mm flux of the filament shown in the naturally-weighted image of Fig. 2 is ∼149 mJy which corresponds with the same assumptions ($\kappa_{3.2\rm mm} \sim 0.17\,\rm cm^2\,g^{-1}$) to a total mass of ∼2200 $\rm M_\odot$. Hence, in this case even naturally-weighted interferometer data recover between 29% to 55% of the single-dish flux and hence resemble the overall structure very well.

We extracted also the peak $S_{\rm peak}$ and integrated fluxes $S_{\rm int}$ of the 12 substructures identified in Fig. 2 (left panel), which are listed in Table 1. These 12 regions were identified by eye with the goal to encompass major structures along the filament. For source identification and flux extraction we used mainly the naturally weighted image (Fig. 2 left panel). We restricted ourselves to structures that are detected above a 4σ level also in the uniformly-weighted image in Fig. 2 (right panel). Obviously, some of these regions can fragment at smaller scales which is already visible for the northernmost peak 1, or also for peak 7 in the uniformly-weighted image. Also extended structures in Fig. 2 (left panel), e.g., between peaks 6 and 7 may be separate fragments (see Fig. 2 right panel), however, they cannot be resolved as individual peaks in the naturally weighted image and are hence not separately extracted. Emission was integrated above the 3σ level of the naturally-weighted image (Fig. 2 left panel), the separation between sources were estimated by eye, usually in emission troughs approximately in the middle between adjacent cores. While the peak positions and hence peak column densities are well defined (Table 1), defining exact boundaries between cores is less straightforward (e.g., Kainulainen et al. 2009; Pineda et al. 2009). Nevertheless, in this rather linear structure of the IRDC 18223 filament, small shifts of boundaries between cores only marginally affect the integrated fluxes and hence estimated masses. Assuming optically thin dust continuum emission at 15 K temperature, the masses M and column densities $N_{\rm H_2}$ corresponding to $S_{\rm int}$ and $S_{\rm peak}$ are also compiled in Table 1. Furthermore, for a better comparison with the virial masses below we calculate the peak masses $M_{\rm peak}$ from the peak column densities $N_{\rm H_2}$ over the size of the beam (Table 3). For region 2, we also calculate the masses and column densities at a higher temperature of 31 K as derived in Beuther et al. (2010). The fragment masses span a broad range between 13 and 843 $\rm M_\odot$, and the column densities range between 9×10^{23} and $1.6 \times 10^{24}\,\rm cm^{-2}$, corresponding to visual extinctions between approximately 100 and 1000 mag, well within the regime of the precursors of high-mass stars (e.g., Kauffmann & Pillai 2010). Table 1 also gives the luminosities derived for individual cores based on Herschel data by Ragan et al. (2012). These luminosities range from starless cores without any far-infrared detections and hence no measurable luminosities, via low-luminosity sources around 100 $L_\odot$ up to almost 2000 $\rm L_\odot$ from the high-mass protostellar object source 2. One should keep in mind that the measured luminosities are bolometric luminosities and do not necessarily stem from hydrogen burning but are likely still dominated by accretion luminosity. The corresponding mass and column density sensitivities estimated from our 3σ flux level of 0.39 mJy beam^{-1} are ∼5.8 $\rm M_\odot$ and ∼6.1×10^{22} cm^{-2}, respectively. Two of the regions are well-studied star-forming objects: core 2 corresponds to IRAS 18223-1243 (Sridharan et al. 2002) and core 10 is the younger high mass protostellar object IRDC18223-3 (Beuther & Steinacker 2007; Fallscheer et al. 2009).

Assuming spherical symmetry within our beam size, the above estimated 3σ column density sensitivity of ≥6.1×10^{22} cm^{-2} results in an approximate density sensitivity of ≥2.6×10^5 cm^{-3}. Combining this density sensitivity with the missing flux ratio, we can estimate a dense gas mass fraction above that density threshold between ∼29% and 55%. Assuming for the dense gas a star formation efficiency of ∼30% (e.g., Alves et al. 2007; André et al. 2014), this results in an approximate overall star formation efficiency of the whole filamentary cloud of 8.7% to 16.5%. These latter values depend strongly on the star formation efficiency which may vary between 20% and 40% (André et al. 2014).

Table 2. Peak separations between mm continuum peaks

peak pairs	peak separations pc
1-2	0.56
2-3	0.55
3-4	0.30
4-5	0.19
5–6	0.33
6–7	0.49
7–8	0.26
8–9	0.19
9–10	0.24
10–11	0.53
11–12	0.70

Another important parameter for the fragmentation processes is the separation between the fragments along the filament. While individual gas cores along the filament may fragment on even smaller scales beyond our spatial resolution and mass sensitivity limits, here we focus on the fragmentation of the filament itself. Table 2 shows the projected separations be-

[2] Typical errors are dominated by the dust model and temperature uncertainties and range within a factor ∼2 (e.g., Ossenkopf & Henning 1994; Beuther et al. 2002.

[3] For this new estimate we used a newly reduced data product provided by the EPOS (Early Phase Of Star Formation) Key-Project team.

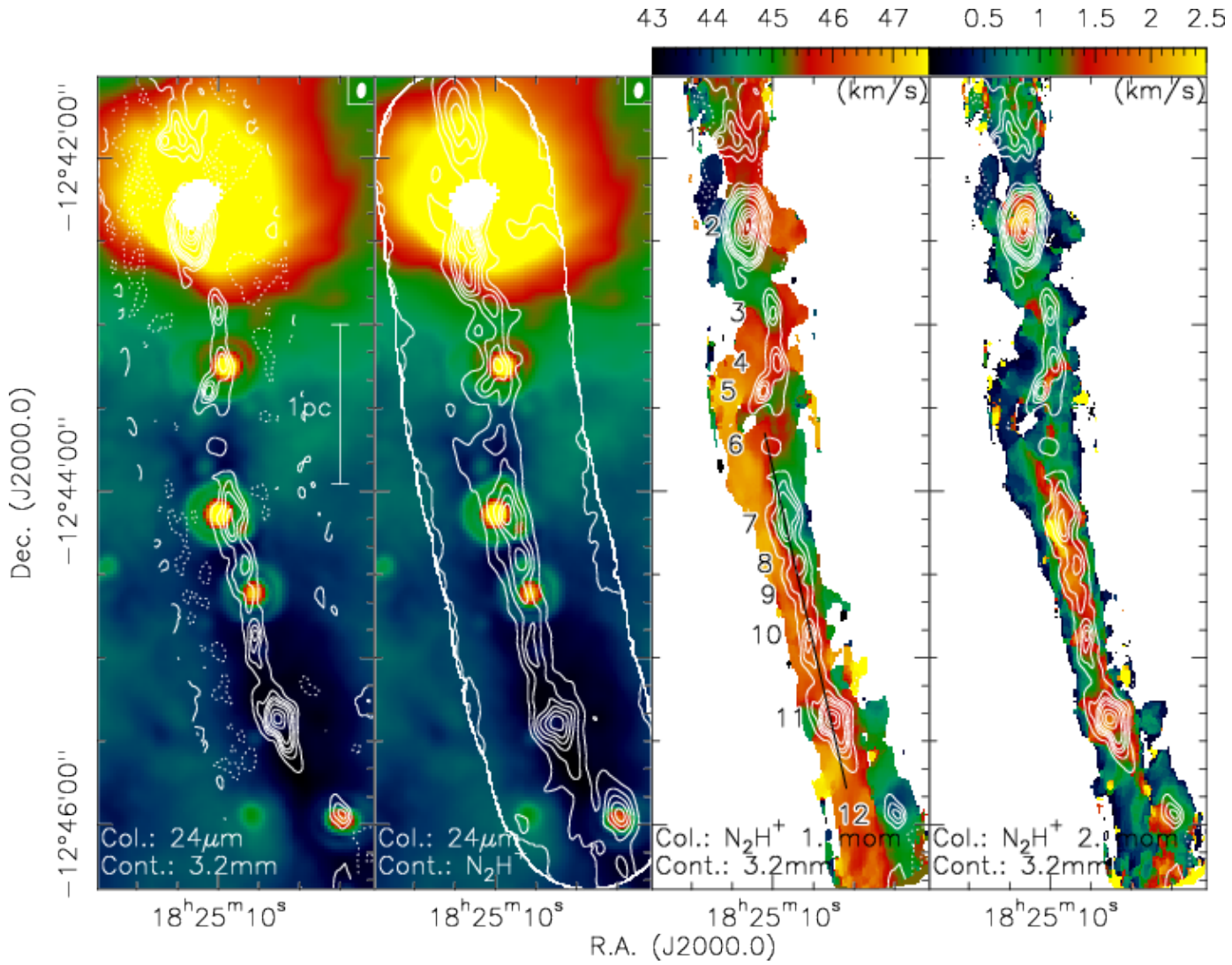

Fig. 3. The left and 2nd panel show the Spitzer 24 μm emission in color with a stretch to increase the visibility of the mid-infrared dark filament. The left panel presents in contours the 3.2 mm continuum emission with natural weighting and the same levels as in Fig. 2. For comparison, the 2nd panel shows in contours the integrated $N_2H^+(1-0)$ emission covering all hyperfine structure components between 35 and 55 km s^{-1}. The third and 4th panel present the 1st and 2nd moment maps (intensity-weighted peak velocities and line-width) extracted from the isolated most negative hyperfine structure component. In the 3rd panel, the velocities are shifted by the separation of the hyperfine structure line of 8 km s^{-1} to the $v_{\rm lsr}$. The contours in the 3rd and 4th panel both show the same continuum contours as in the left panel. The black line in panel 3 gives the direction of the position-velocity cut shown in Fig. 6. A scale-bar is depicted in the left panel.

tween the 12 cores identified in Fig. 2 and Table 1. These values result in a mean projected separation between the fragments of ~0.40 pc with a standard deviation of 0.18 pc. This mean separation should be considered as an upper limit because more fragments along the filament may exist that were not identified within the spatial resolution and mass sensitivity of our data. For comparison, we can estimate the Jeans length for mean densities of the large-scale filament between 10^4 and 10^5 cm^{-3} at 15 K to a range between ~0.23 and ~0.07 pc. These Jeans scales are considerably smaller than the observed mean fragment separation. Although the measured fragment separations are projected upper limits, a difference of more than a factor of 2 between measurements and Jeans lengths appears significant. We will discuss this result in the context of filament fragmentation in section 4.1.

Furthermore, the mass-to-length ratio M/l can be compared to the critical mass per length $M/l_{\rm crit}$ in an equilibrium situation (e.g., Ostriker 1964; Fiege & Pudritz 2000a,b). Deviations from this $M/l_{\rm crit}$ indicate non-equilibrium modes. While filaments with line masses below $M/l_{\rm crit}$ expand if not supported by external pressure, filaments with line masses strongly exceeding $M/l_{\rm crit}$ can collapse radially perpendicular to the main long axis of the filament. Such radial collapse would be on very short timescales and hence prohibit further fragmentation along the main axis of the filament (e.g., Inutsuka & Miyama 1992). If turbulent pressure dominates over thermal pressure, using ~2.5 km s^{-1} as an approximate line width from the single-dish data for the dense gas of the IRDC 18223 filament (Fig. 1, third panel 2nd moment map), one can estimate a critical mass to length ratio $(M/l)_{\rm crit-turb} \approx 84 \times (\delta v)^2 \approx 525\,{\rm M}_\odot\,{\rm pc}^{-1}$ (e.g., Jackson et al. 2010), more than 20 times higher than the $(M/l)_{\rm crit-therm} \approx 25\,{\rm M}_\odot\,{\rm pc}^{-1}$ for an undisturbed filament using the thermal sound speed at 15 K of 0.23 km s^{-1} (Ostriker 1964).

Table 1. Fluxes, masses, column densities (at 15 K) and luminosities of the individual cores

#	R.A.	Dec.	$S_{\rm peak}$[a]	$S_{\rm int}$[a]	$N_{\rm H_2}$	$M^e_{\rm peak}$	M	L^c
	(J2000.0)	(J2000.0)	$\left(\frac{\rm mJy}{\rm beam}\right)$	(mJy)	$(\frac{10^{23}}{\rm cm^2})$	($\rm M_\odot$)	($\rm M_\odot$)	($\rm L_\odot$)
1[b]	18:25:11.11	-12:41:52.8	1.5	8.3	2.3	22	123	157
2	18:25:10.61	-12:42:25.0	10.3	57.0	16.0	150	843	1979
2[d]					7.2	77	377	
3	18:25:09.99	-12:42:56.1	1.4	3.1	2.2	20	46	
4	18:25:09.91	-12:43:14.0	1.5	4.1	2.3	22	61	135
5	18:25:10.21	-12:43:24.2	2.0	5.1	3.1	29	75	
6	18:25:10.04	-12:43:43.6	0.6	0.9	0.9	9	13	
7	18:25:09.69	-12:44:12.1	1.8	12.0	2.8	26	177	201
8	18:25:09.31	-12:44:26.4	1.6	6.3	2.5	23	93	
9	18:25:09.23	-12:44:37.6	1.0	2.4	1.6	15	36	
10	18:25:09.09	-12:44:52.0	1.7	6.9	2.6	25	102	
11	18:25:08.49	-12:45:22.0	6.7	26.0	10.4	97	385	324
12	18:25:06.94	-12:45:56.7	1.3	2.4	2.0	19	36	79

[a] Peak and integrated fluxes are extracted from the naturally-weighted 3.2 mm continuum image within the 3σ contours.
[b] This is the approximate mid-point between the three sub-peaks there.
[c] From Ragan et al. (2012).
[d] Calculated also at 31 K following Beuther et al. (2010).
[e] Peak masses $M_{\rm peak}$ are calculated from the peak column densities $N_{\rm H_2}$ for a more accurate comparison with virial masses measured toward the peak positions (Table 3).

For comparison, we can estimate the M/l of the IRDC 18223 filament by dividing the total filament mass estimated from the 1.2 mm MAMBO data of $\sim$4000 $\rm M_\odot$ by the projected length of the total filament of $\sim$4 pc. This results in a very high M/l of 1000 $\rm M_\odot\,pc^{-1}$. Although larger than the estimated $(M/l)_{\rm crit-turb}$, the difference of about a factor 2 is within the uncertainties considering that the linewidth is squared in the equation above. Hence, turbulent motions may help stabilizing the filament against fast radial collapse. One should keep in mind that turbulence can also create shocks and by that density enhancements and filaments. In addition to this, magnetic fields may help to stabilize the filament as well. For example, recent magneto-hydrodynamic (MHD) simulations by Kirk et al. (2015) showed that in their MHD case the $M/l_{\rm crit-B}$ increased by a factor of $\sim$3 compared to the pure hydro case. Although radial collapse cannot be entirely excluded, the fact of the existence of this filament with such a regular fragment separation as well as the large $(M/l)_{\rm crit-turb}$ make radial collapse a less likely scenario.

3.2. The gas kinematics of the filament

Figure 3 presents a compilation of the $N_2H^+(1-0)$ emission in comparison to the 3.2 mm cold dust continuum as well as the 24 μm mid-infrared warm dust emission/absorption. The dense gas tracer N_2H^+ follows the filamentary structure very well with the integrated emission peaks showing close resemblance to the peak positions in the 3.2 mm continuum (Fig. 3, 1st and 2nd panel). The line emission seems even to trace the larger-scale structure slightly better than the continuum observations.

The third panel in Fig. 3 presents a first moment map (intensity-weighted peak velocities) of the whole filament (conducted with the isolated hyperfine structure component shifted by 8 $\rm km\,s^{-1}$ to the $v_{\rm lsr}$). While the combined optical depth of all hyperfine components together often exceeds 1 toward the main core peak positions (e.g., Fig. 5), the moment maps are done with the isolated hyperfine component 8 $\rm km\,s^{-1}$ apart from the main component at a relative intensity of $\sim$11%, hence at optical depth $\ll 1$. Therefore, the peak velocities in Fig. 3 should not be affected by optical depth effects. The northern part of the region between peak 1 and 5 does shows some variation between red- and blue-shifted gas without any clear signature along or across the filament. In particular, one can identify a clear velocity gradient across core 2 in the north. However, since that is a well-known high-mass protostellar object likely driving a molecular outflow (Sridharan et al. 2002), this velocity structure is likely strongly influenced by the dynamics of the already more evolved internal source. The situation is different from peak 6 southward. In this southern part, the first moment map is indicative of a velocity gradient across the filament from red-shifted gas in the east to blue-shifted gas in the west. Conducting a cut perpendicular to the filament through continuum source 8 in Fig. 3, we measure peak velocities between 44.8 and 47.0 $\rm km\,s^{-1}$ over an angular size of $\sim$15″, corresponding to $\sim$0.26 pc at the given distance, corresponding to a velocity gradient of $\sim$25.6 $\rm km\,s^{-1}\,pc^{-1}$. The velocity gradient can also be seen by inspecting the channel map of the gas (Fig. 4). The almost vertical line in the channel map is drawn to guide the eye along the filamentary structure seen in the channel at 47.2 $\rm km\,s^{-1}$. This channel map also shows that at redshifted velocities the gas in the south is located further to the east than at blue-shifted velocities. An exception is the emission of peak 10 (also known as IRDC 18223-3) which covers almost the entire velocity range. This peak is clearly more evolved than the other fragments and also drives an energetic outflow (Fallscheer et al. 2009). Fig. 3 also presents a second moment map (intensity-weighted line width) which shows a line width increase toward the ridge of the filament often closely related to the mm continuum emission. While some of this increased line width is clearly associated with star formation activity (e.g., peaks 2 and 10 also known as IRAS18223-1243 and IRDC 18223-3), in other cases, this second moment increase can also be caused by multiple velocity components (see below).

One can now ask whether this more than 2 pc long southern part of the filament is either a velocity-coherent structure with only a small velocity-gradient from east to west, or whether it may consist of several sub-filaments that may form the large structure (e.g., Hacar et al. 2013; Smith et al. 2014). To analyze this in more detail, Fig. 5 presents the $N_2H^+(1-0)$ spectra extracted toward the 12 mm peak positions. For all spectra we fitted the full hyperfine structure with either one or two spectral velocity components. The decision to fit either single or multi-

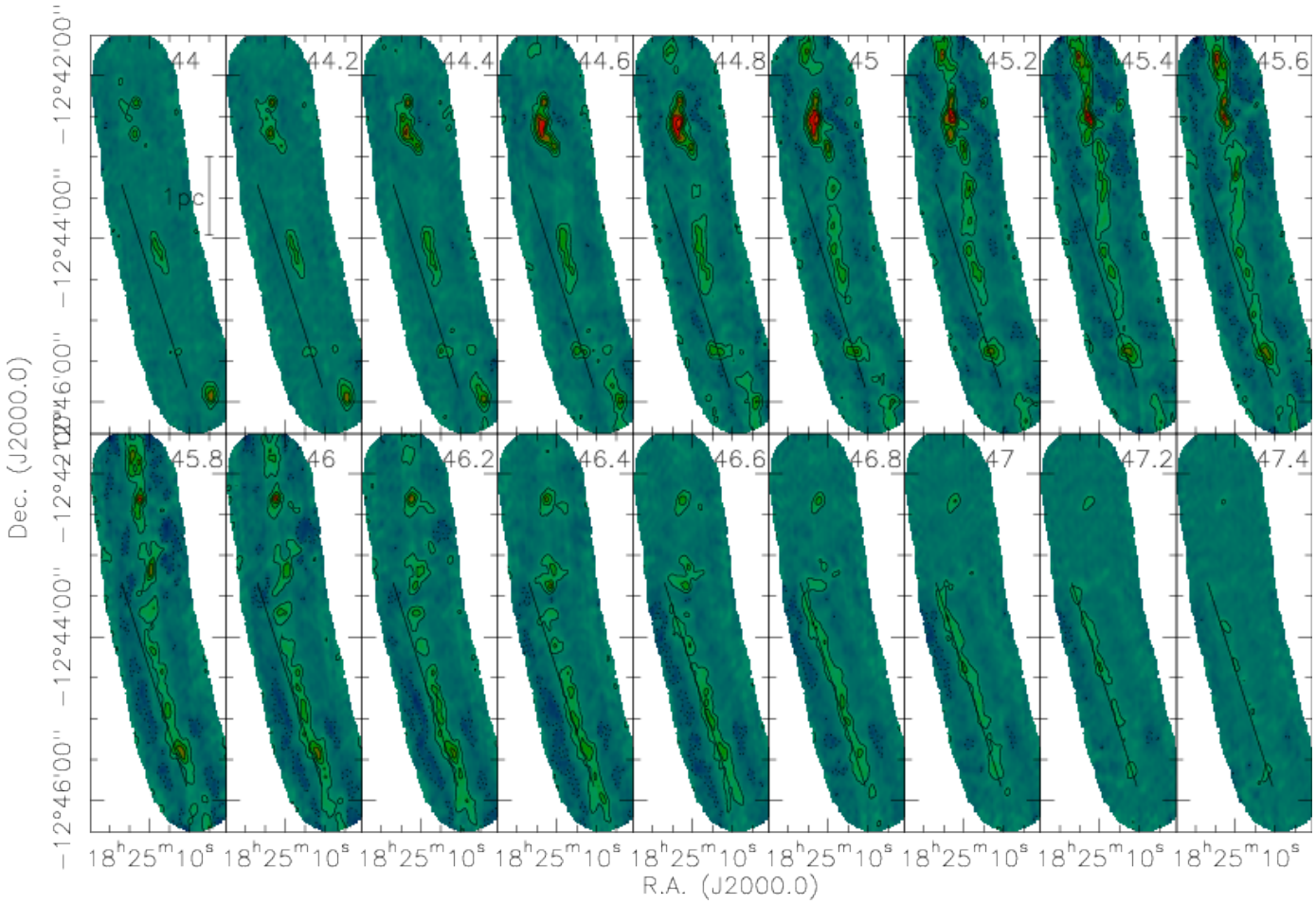

Fig. 4. Channel map of the isolated component of the $N_2H^+(1-0)$ line. The velocities are shifted by the separation of the hyperfine structure line of 8 km s^{-1} to the $v_{\rm lsr}$. Velocities for each channel are given in the top-right of each panel. The contours in each panel are from 5 to 95% of the respective peak emission in that channel. Negative features at the same contour levels are shown in dashed lines. A linear scale bar is presented in the top-left panel. The line is meant to guide the eye and is drawn along the main filamentary structure visible in the channel at 47.2 km s^{-1}.

ple components was mainly based on the shape of the isolated most-blueshifted hyperfine structure line component. The fit results are shown in Table 3 and in Figure 5. More than 50% of the spectra clearly need two velocity components to adequately fit the data (e.g., mm2 and mm7, even the spectrum toward peak 10 is likely an overlap of multiple components potentially caused by the internal outflow-driving source). It is interesting to note that most of the single component fits as well as often one of the two components exhibit relatively narrow line width below 1 km s^{-1}. Nevertheless, although comparably narrow, even these components have significant non-thermal contributions since the thermal line width of N_2H^+ at 15 K is ∼0.15 km s^{-1}. The second component usually is slightly broader between 1.3 and 2.7 km s^{-1}. These broader components may also be comprised out of multiple components along the line of sight.

The peak velocities extracted from the spectra do not exhibit a clear velocity gradient along the filament. Therefore, in contrast to the velocity-gradient seen in the moment map from east to west, there is no obvious velocity gradient from north to south along the filament. As already mentioned for the whole filament, this missing gradient along the filament may either be due to missing significant streaming motions along, or it may also be introduced due to a possible orientation almost in the plane of the sky.

The measured line width toward the individual peak positions can also be used to get a rough estimate of the virial mass of the individual fragments. Following MacLaren et al. (1988), we estimate the virial mass according to $M_{\rm vir} = k_2 \times R \times \Delta v^2$, where we use $k_2 = 126$ for a $\rho \propto r^{-2}$ density distribution, $R = 16000$ AU∼ 0.078 pc the size of the region corresponding to the beam size of the $N_2H^+(1-0)$ data, and the measured full width half maximum Δv. The resulting virial masses $M_{\rm vir}$ are shown in Table 3. A direct correlation with the masses derived from the dust emission in Table 1 is not possible because some sources have more than one N_2H^+ component and thus several virial mass estimates, whereas the gas masses from the continuum emission are always single values. Nevertheless, in most cases of multiple velocity components, one dominates. Table 3 also shows the ratio of the virial masses divided by the peak masses $M_{\rm peak}$ derived from the peak column densities $N_{\rm H_2}$ in Table 1. While in a majority of cases this $M_{\rm vir}/M_{\rm peak}$ ratio is considerably smaller than 1, there are also several cases where the ratio is close to unity or even higher. Interestingly, the three highest $M_{\rm vir}/M_{\rm peak}$ sources 4, 5, and 6 show very different internal luminosity characteristics. While source 4 has a clear asso-

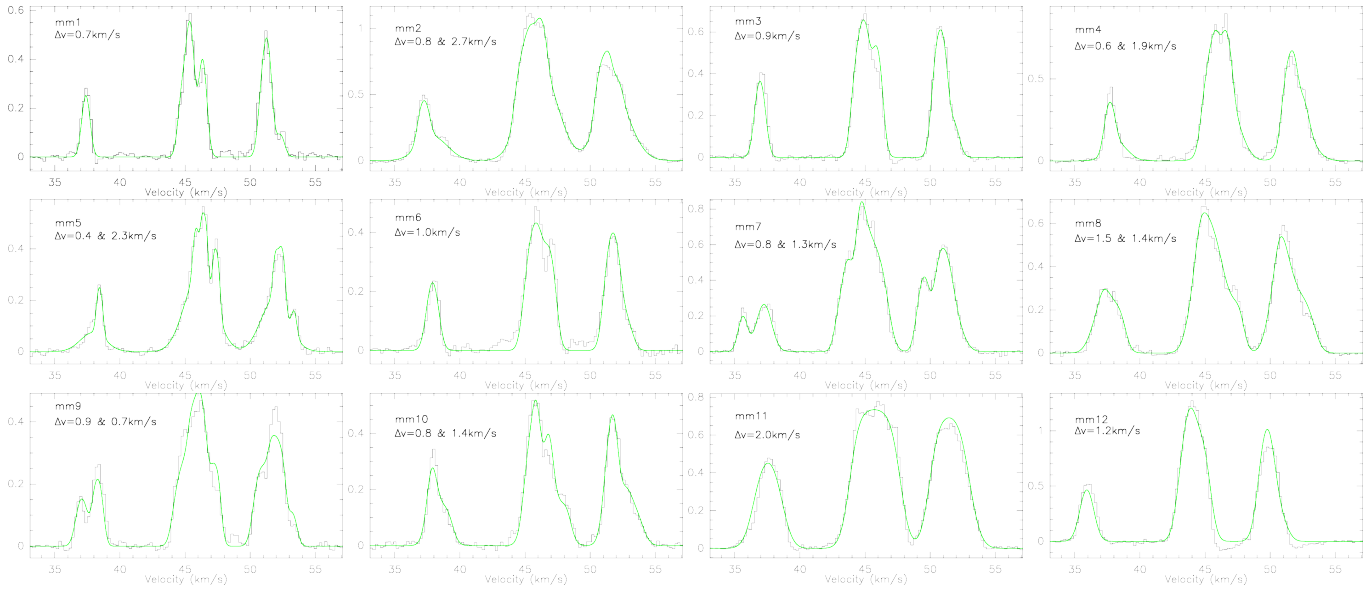

Fig. 5. Spectra and hyperfine structure line fits towards the 12 positions marked in Fig. 2 and Table 1. The y-axis is in units of Jy beam^{-1}. The full width half maximum values of single- or double-component fits are shown in each panel.

ciated internal heating source, #5 is at the edge of that, and #6 exhibits no detectable 24 μm emission (Fig. 3). From a virial balance point of view, this comparison is an indicator that many of the individual cores are prone to collapse or already collapsing (see also recent filament work by Battersby et al. 2014). The latter is also evident by embedded sources within many of the dust continuum peaks (e.g., Fig. 1 left and right, mid- to far-infrared panels). However, there are exceptions which may still be stable against gravitational collapse (e.g., source 6).

Table 3. $N_2H^+(1-0)$ hyperfine structure line fits

#	$v_{\rm peak}$ (km s^{-1})	Δv (km s^{-1})	$M_{\rm vir}$ ($M_\odot$)	$\frac{M_{\rm vir}}{M_{\rm peak}}$ [b]
1	45.4	0.7	4.8	0.22
2	45.2	0.8	6.3	–[c]
	45.9	2.7	71.3	0.92
3	44.9	0.9	7.9	0.36
4	45.7	0.6	3.5	–[c]
	46.1	1.9	35.3	1.60
5	45.9	2.3	51.7	1.78
	46.4	0.4	1.6	–[c]
6	45.9	1.0	9.8	1.09
7	43.6	0.8	6.3	0.24
	45.2	1.3	16.5	0.63
8	44.8	1.5	22.0	0.96
	45.9	1.4	19.2	0.82
9	45.1	0.9	8.0	0.53
	46.3	0.7	6.3	0.42
10	45.9	0.8	6.3	0.25
	46.4	1.4	19.2	0.77
11	45.6	2.0	39.1	0.40
12	43.9	1.2	14.1	0.74

[a] Peak velocities and FWHM values from fits to full hyperfine structure
[b] $M_{\rm peak}$ are taken from the continuum data in Table 1.
[c] The line widths and virial masses of these secondary velocity components are negligible compared to the main components.

A different way to look at the velocity structure is a position-velocity cut along the southern filament. Figure 6 presents such a position-velocity (pv) diagram going from south to north between peaks 11 and 6 as outlined in Figure 3. While this pv cut exhibits very broad emission in the south toward peak 11 (or IRDC 18223-3) which is also visible in Figs. 4 & 5, the rest of the cut does show a variety of features: while some peaks exhibit single emission peaks redshifted with respect to the $v_{\rm lsr}$ (e.g., peak 10 or 6), others show multiple peaks on both sides of the $v_{\rm lsr}$ (e.g., peaks 7 to 9). Again, no clear velocity gradient across the structure can be identified. However, the position-velocity cut shows that internal structure is found within this filament. As outlined in section 3.1, our identified fragments within the filament (Table 1) represent likely only a lower limit to the actual structures, and more fragments may exist. For example, in Fig. 6 we can identify structures between peaks 6 and 7. Comparing these to the continuum maps in Fig. 2, they are spatially close to the extended structures in Fig. 2 (left panel) and the 4σ peaks in Fig. 2 (right panel).

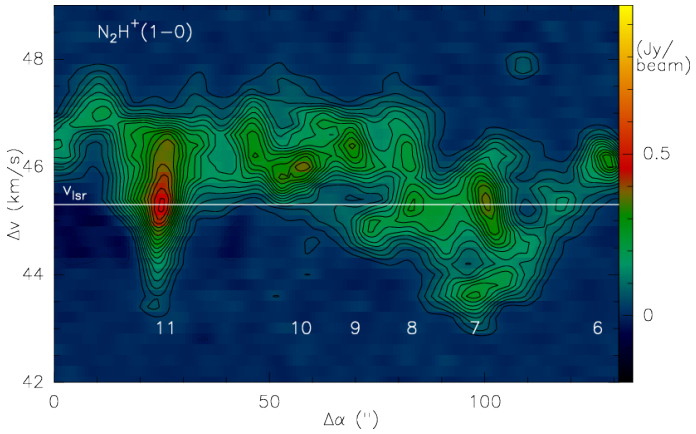

Fig. 6. Position-velocity cut through the southern half of the filament in the isolated $N_2H^+(1-0)$ line (shifted to the $v_{\rm lsr}$) from south to north along the axis shown as black line in panel 3 of Fig. 3. The mm peak names are marked at the bottom.

A natural question is whether similar kinematic features can be found in the less dense surrounding of the gas on larger spatial scales. In a recent [CII]/[CI]/$C^{18}O$ emission line study toward four IRDCs, Beuther et al. (2014) identified several velocity components between 42 and 56 km s^{-1} in comparably localized emission structures in the atomic and molecular carbon emission east of the IRDC 18223 filament. To investigate this in more detail, we used the atomic [CI] and molecular $C^{18}O$(2–1) data of the region (Beuther et al. 2014). Figure 7 shows the first moment maps of these tracers toward our target region. In these moment maps, for both tracers no obvious large-scale velocity gradients across the filament can be identified. The only mentionable feature in Fig. 7 is that the dense filament seem in $C^{18}O$ and [CI] appears to be slightly blue-shifted compared to the larger scale molecular cloud. This effect is more pronounced in the $C^{18}O$(2–1) than the [CI] emission. For comparison, we extracted the $C^{18}O$(2–1) spectra toward five positions across the filament at the declination of mm continuum source 8 (Fig. 8). Toward the central positions, these spectra show that the two N_2H^+ velocity components are approximately recovered in the $C^{18}O$ emission as well. This indicates that, if the region were observed at higher angular resolution also in $C^{18}O$, one would likely identify similar velocity structures as in N_2H^+. Moving outward to the east, the emission becomes more redshifted whereas to the west the emission is more blueshifted. This is particularly prominent in the spectra at +60″ and −60″ (corresponding to ∼ ±1 pc, Fig. 8), respectively. Interestingly, this velocity shift found in the individual spectra is hard to identify in the moment maps because several components overlap diminishing the signatures this way. It should be noted that the velocity gradient found this way on large scales for the cloud is considerably smaller than the 25.6 km s^{-1} pc^{-1} found above for the dense filament in the interferometric N_2H^+ data. While it appears in general plausible that the velocities increase when going to higher densities, recent molecular cloud and filament formation simulations tend to find similar signatures (e.g., Moeckel & Burkert 2015; Smith et al. 2015). This trend needs to be investigated more in the future from an observational as well as theoretical point of view. Nevertheless, the general trend of redshifted gas in the east and blueshifted gas in the west is found on the large scales traced by the $C^{18}O$ single-dish emission as well as on the small scales studied with the new PdBI N_2H^+ data. Hence, we find tentative evidence that the large-scale cloud and the smaller-scale filament are kinematically coupled.

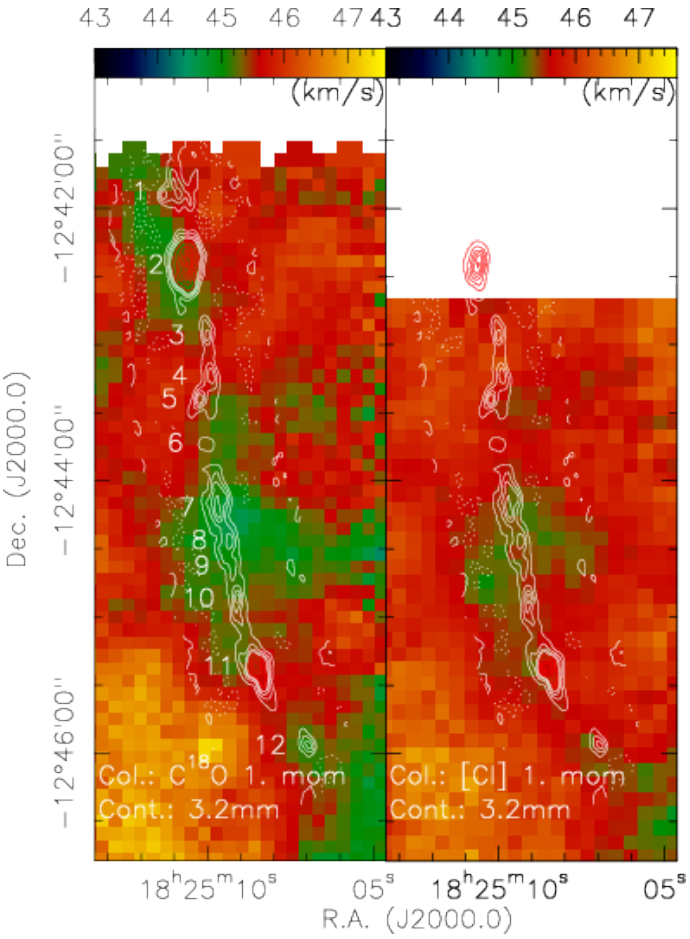

Fig. 7. The two panels show for comparison the first moment maps in molecular $C^{18}O$(2–1) and atomic carbon [CI] obtained from the IRAM 30m and APEX data presented in Beuther et al. (2014). The contours are the 3.2 mm continuum emission with natural weighting and the same levels as in Fig. 2. The numbers of the mm cores are given in the left panel.

4. Discussion

4.1. Filament fragmentation

As outlined in Section 3.1, the separations between the main identified fragments along the filament exceed the Jeans length at the given densities and temperatures. Although our measured projected separations are upper limits because of potential unresolved fragmentation and/or fragments below our sensitivity limit, the difference between Jeans length and projected fragment separation by more than a factor two appears significant. As a next step, we analyze the region in the framework of isothermal, gravitationally bound gaseous cylinders. Based on early work of Chandrasekhar & Fermi (1953); Nagasawa (1987) and Inutsuka & Miyama (1992) as well as more recent adaptions like Jackson et al. (2010), Beuther et al. (2011) or Kainulainen et al. (2013), we study the conditions of an infinite isothermal gas cylinder. Although IRDC 18223 is obviously not of infinite length, the filament is part of a much larger structure extending more than 50 pc projected on the sky. Hence, in this context, the approximation of IRDC 18223 being part of a much longer, almost infinite structure seems justifiable. Furthermore, since star formation has already started at different locations in the filament, it is not the perfect starless filament anymore. However, the infrared dark nature of IRDC 18223 clearly shows the youth of the whole structure. Hence, it is still an excellent target region that represents conditions in the relatively early phase of filament fragmentation.

This characteristic isothermal scale-height H of such a gas cylinder is given by $H = c_s(4\pi G\rho)^{-1/2}$ with c_s the sound speed, G the gravitational constant and ρ the gas mass density at the center of the filament (e.g., Nagasawa 1987). With a thermal sound speed of the gas at 15K of $c_s \sim 0.23$ km s^1 and using an approximate density $\rho \sim 10^5$ cm^{-3} (e.g., Beuther et al. 2002), the characteristic scale-height is $H \sim 0.02$ pc. In that case, the characteristic fragmentation scale corresponding to the fastest growing unstable mode of the fluid instability is $\lambda_{\rm frag} = 22H$ (e.g., Nagasawa 1987; Inutsuka & Miyama 1992; Jackson et al. 2010) which results with the above used parameters for the sound speed and the temperature in an approximate fragmentation scale $\lambda_{\rm frag} \approx 0.44$ pc. One should keep in mind that there are uncertainties associated with the assumed density and sound speed, which introduce an uncertainty in the estimated core separation.

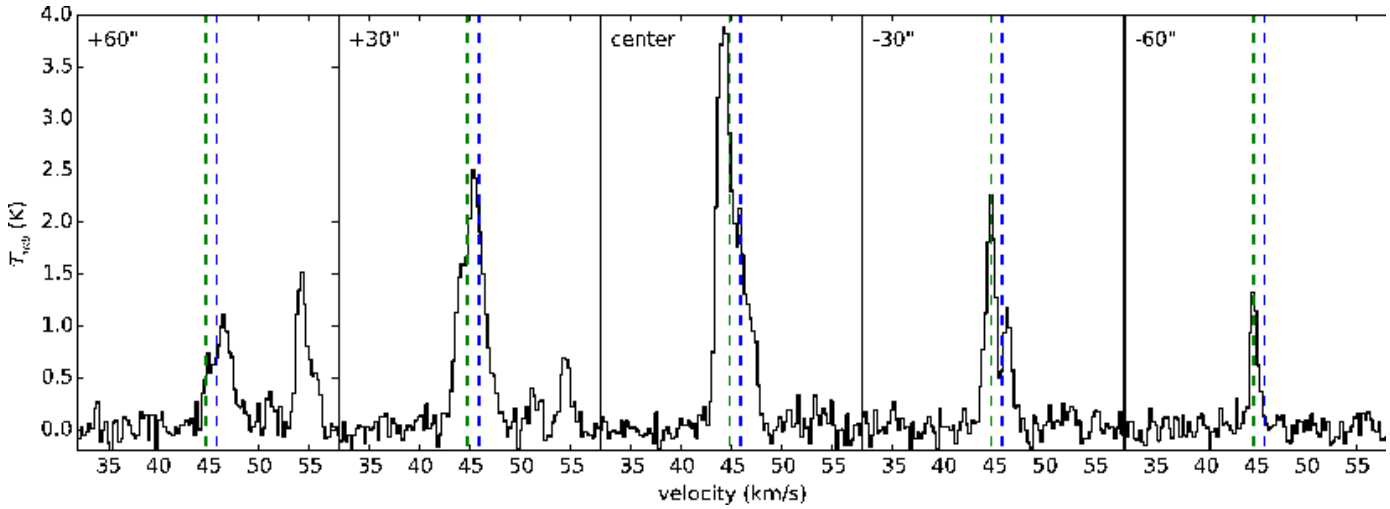

Fig. 8. $C^{18}O(2–1)$ spectra from the IRAM 30m telescope extracted along a cut perpendicular to the filament at a declination of mm continuum source 8 (Beuther et al. 2014, Ragan et al. in prep.). The green and blue vertical lines mark the two velocity components measured in $N_2H^+(1–0)$ toward the central source 8. The R.A. offsets are marked in each panel.

In particular, instead of the thermal sound speed of the gas, other works have used the Gaussian turbulent velocity dispersion in this estimate, which would increase the estimated value for $\lambda_{\rm frag}$ according to the ratio of the turbulent velocity dispersion over the thermal sound speed (e.g., Wang et al. 2014). Nevertheless, it is interesting to note that using the thermal sound speed at 15 K and an approximate central density of 10^5 cm^{-3} results in $\lambda_{\rm frag}$ which is close to the mean core separation of the filament of ∼0.40 pc discussed in section 3.1. Although our observed mean separation is likely only an upper limit (Section 3.1), an isothermal, gravitationally bound and compressible gas cylinder allows us to reproduce the general fragmentation structure of IRDC 18223 well.

The high mass-to-length ratio estimated from the dense gas bolometer single-dish data of M/l of ∼1000 M$_\odot$ pc^{-1} exceeds by far the critical mass to length ratios for thermal filaments, but it is approximately consistent with a scenario where also turbulent support of the filament against radial collapse is considered (Section 3.1). Additional effects, e.g., the presence of magnetic fields may add further support to the stability of the filament. The recent MHD simulations by Kirk et al. (2015) revealed an increase of the critical mass-to-length ratio by a factor of ∼3 compared to their pure hydrodynamical simulations. One should keep in mind that only if the filament does not collapse radially perpendicular to the filament, perturbations along the filament can grow and result in fragmentation as discussed above (e.g., Inutsuka & Miyama 1992). Quantitatively speaking, it is one of the largest M/l values found so far, where Nessie is reported with ∼110 M$_\odot$ pc^{-1}, Orion with 385 M$_\odot$ pc^{-1} (Bally et al. 1987; Jackson et al. 2010), a sub-filament in the G35.39 region with 115 M$_\odot$ pc^{-1} (Henshaw et al. 2014), and the G11.11 IRDC with a value of 600 M$_\odot$ pc^{-1} (Kainulainen et al. 2013).

4.2. Kinematics of the filament

The kinematic properties of filaments have recently been discussed in a different context. Signatures of gas flows along the filaments have been identified (e.g., Hacar & Tafalla 2011; Kirk et al. 2013; Tackenberg et al. 2014; Zhang et al. 2015), and velocity coherent sub-structures have been identified that may originate from the filament formation process (e.g., Hacar et al. 2013; Smith et al. 2014; Henshaw et al. 2014). Furthermore, recently velocity gradients perpendicular to filaments were discussed that may also be signatures of filament formation (Fernández-López et al. 2014).

Potential signatures for gas flows along the filament are blue-red-shifted velocity structures on the two opposite sites of mm peak positions, indicating that the gravitational well of the gas peaks attracts the gas from the filament. While we cannot exclude such a possibility, the moment maps and position-velocity diagrams (Figs. 3 & 6) at least show no obvious signatures of this. The fact that we do not see any strong gradient from north to south could be due either to barely any streaming motions along the filament, or it can also indicate that the filament may be oriented relatively close to the plane of the sky. Such a low inclination angle would make any identification of gas flows along the filament very difficult.

Another signature of gas flows along the filament could be regular oscillatory-like velocity changes along such a filament as discussed in Hacar & Tafalla (2011) or Zhang et al. (2015). While the pv-cut in Figure 6 shows velocity fluctuations around the $v_{\rm lsr}$, it is hard to identify such a sea-saw pattern. Therefore, this signature is also not evident in our data.

In a recent study of the filaments in Serpens south, Fernández-López et al. (2014) find velocity gradients perpendicular to filaments as well, very similar to our findings here. Although they also find velocity-gradients along the filaments, they stress that the velocity-gradients perpendicular to the filaments are about an order of magnitude larger than those along the filaments. The quantitative gradients they derive perpendicular and parallel to the filament are 11.9 km s^{-1} pc^{-1} versus 0.9 km s^{-1} pc^{-1}, respectively. This is suggestive for the kinematics perpendicular to the filaments being dynamically much more important than those along the filaments. The gradient we find in IRDC 18223 is even larger with ∼25.6 km s^{-1} pc^{-1}. Although Fernández-López et al. (2014) postpone a more detailed comparison with simulations to a future paper (Mundy et al. in prep.), the main thrust of their interpretation is that such velocity-gradients perpendicular to filaments may stem from motions associated with the formation and growing of the filaments (see also Heitsch 2013a,b). Hence they may be direct signatures of the filament formation processes. Similar results are

also indicated by recent three-dimensional simulations of turbulence compressed regions in strongly-magnetized sheet-like layers (Chen et al. 2015). Within these layers, dense filaments and embedded self-gravitating cores form via gathering or compression of the material along the magnetic field lines. As a result of the mass collection along preferred directions, velocity gradients perpendicular to the filament major axis are a common feature seen in their simulations (Chen et al. 2015).

Regarding velocity-coherent sub-filaments, the velocity shifts of the southern part of the filament, particularly prominent in the channel map (Fig. 4), allows us to speculate whether we have also in this region similar structures. While in principle rotation of the filament is a possible explanation for the observed spectral signatures, Kirk et al. (2013) showed that for an accreting filament, infall motions would quickly dominate the kinematics, even if the filament were initially rotating. In Fig. 6, one can tentatively identify several contiguous regions in space/velocity between offsets $\sim$ 40″ and $\sim$ 80″ (peaks 9 and 8) and a velocity of $\sim$ 46 km s^{-1}, as well as between $\sim$ 70″ and $\sim$ 120″ (midway between peaks 8/9 and midway between peaks 6/7) and a velocity of $\sim$ 45 km s^{-1}. While Hacar et al. (2013) find a large number of bundles of filaments within the Taurus region, Henshaw et al. (2014) identify three sub-filaments within their studied G35.39 dark filament. This latter high-mass infrared dark cloud compares more closely to our IRDC 18223 filament in physical properties (e.g., mass, size, velocity dispersion) . In principle, a series of velocity-coherent sub-filaments could mimic also a velocity gradient across the structure. However, since the observations presented here are interferometer-only data without the missing short-spacing information, an automized search for velocity-coherent fibers in a manner analogous to the studies by Hacar et al. (2013) or Henshaw et al. (2014) is not possible. As mentioned before, the rms and spectral resolution of our currently available Nobeyama 45 m single-dish data is not sufficient for a reasonable merging with the interferometer data. However, we plan to obtain high-quality short-spacing data in the future and revisit the analysis.

Alternative interpretations have recently been invoked to explain observed trends in filament velocity structure. Recently, Tafalla & Hacar (2015) discussed the possibility that the filament in Taurus which they observed may have formed from the supersonic collision of sub-filaments, and that in the next step, this filament will fragment due to gravitational instabilities. Similarly, Smith et al. (2014) recently discussed filament formation by pre-existing structures based on hydrodynamic collapse simulations.

An additionally interesting aspect in the presented results is that the velocity gradient found on small scales in the interferometer data perpendicular to the filament is also found on larger scales by the single-dish $C^{18}O(2–1)$ data (Fig. 8). This indicates that larger-scale diffuse gas is kinematically coupled to the dense inner filament. The fact that we find a significant steeper velocity gradient in the dense inner filament compared to the larger-scale cloud can also be identified in recent cloud and filament formation simulations (e.g., Moeckel & Burkert 2015; Smith et al. 2015).

To summarize, on the spatial scales traced by our interferometer data, the identified velocity-gradient perpendicular to the filament as well as tentatively velocity-coherent sub-structures may both stem from (magnetized) turbulent flows in sheet-like or filamentary structures. Such turbulent and sheet-like substructures could have formed out of the larger-scale self-gravitating and collapsing cloud. Figure 9 sketches the approximate structure of the region highlighting the main features.

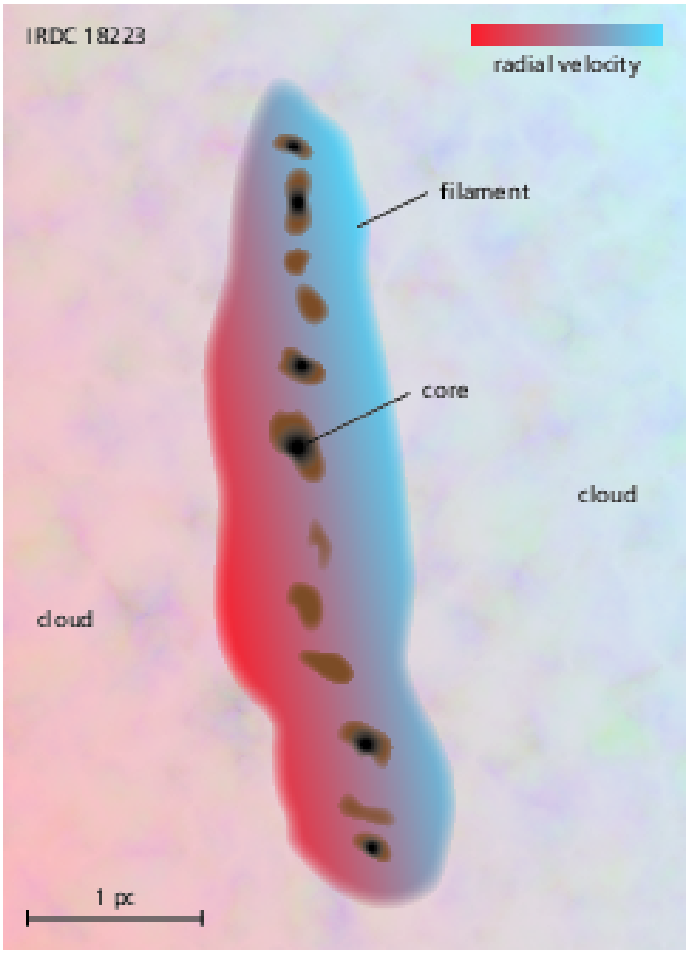

Fig. 9. Sketch of the approximate structure of IRDC 18223.

5. Conclusions

The PdBI 3.2 mm line and continuum emission resolves this more than 4 pc long filament into its substructures at about 15000 AU scale. We identify a linear structure with ~12 cores at approximately similar spacing with a mean projected separation of ~0.40(±0.18) pc. This separation is much larger than the typical Jeans length. Although the observed core separation is an upper limit because of limited spatial resolution and sensitivity, the data are approximately consistent with the fragmentation properties of an isothermal, gravitationally bound and compressible gas cylinder. However, the mass-to-length ratio is also very high implying additional turbulent and/or magnetic support of the filament if it is supported against radial collapse.

We do not find any significant velocity gradient along the 4 pc filamentary structure, but the PdBI $N_2H^+(1-0)$ data reveal a transverse velocity gradient across the southern half of the filament. While it is possible that this southern filament may be composed of at least two velocity-coherent sub-filaments, rotation of the filament cannot be excluded either, although the latter appears less likely. The missing signatures of gas flows along the filament may indicate small streaming motions along the filament but they could also be caused by a low inclination angle of the filament with respect to the plane of the sky.

The velocity gradient perpendicular to the filament may also stem from the filament formation process within magnetized and turbulent sheet-like structures. On scales of ±60″ ($\sim$ ±1 pc) east and west of the filament we find similar red/blueshifted signa-

tures as on the smaller filament scales. This may be tentative evidence that the lower-density cloud and higher-density filament indeed may be kinematically coupled.

In summary, these combined line and continuum data reveal an excellent example of a massive gas filament. While the continuum data are roughly consistent with thermal fragmentation of a cylinder, the high mass-to-length ratio requires additional support against radial collapse, most likely due to turbulence and/or magnetic fields. Furthermore, the observed velocity structure of the gas indicates a dynamic origin of the filament. However, we cannot resolve yet whether it is comprised of individual velocity-coherent sub-filaments or whether other processes like magnetized converging gas flows, a larger-scale collapsing cloud or even cloud rotation play a significant role in the formation process. Future observations combining single-dish and interferometer data will help to better constrain these different scenarios.

Acknowledgements. We like to thank Axel Quetz for helping to produce the sketch in Fig. 9. Furthermore, thanks a lot to Hendrik Linz from the EPOS Key-Project team for providing us a newly reduced version of the Herschel 500 μm data. S.E.R. acknowledges support from VIALACTEA, a Collaborative Project under Framework Programme 7 of the European Union, funded under Contract # 607380.

References

Alves, J., Lombardi, M., & Lada, C. J. 2007, A&A, 462, L17
André, P., Di Francesco, J., Ward-Thompson, D., et al. 2014, in Protostars and Planets VI, ed. H. Beuther, R. Klessen, C. Dullemond, & T. Henning, 27–51
André, P., Men'shchikov, A., Bontemps, S., et al. 2010, A&A, 518, L102
Arzoumanian, D., André, P., Didelon, P., et al. 2011, A&A, 529, L6
Bally, J., Langer, W. D., Stark, A. A., & Wilson, R. W. 1987, ApJ, 312, L45
Battersby, C., Ginsburg, A., Bally, J., et al. 2014, ApJ, 787, 113
Beuther, H., Henning, T., Linz, H., et al. 2010, A&A, 518, L78
Beuther, H., Kainulainen, J., Henning, T., Plume, R., & Heitsch, F. 2011, A&A, 533, A17
Beuther, H., Ragan, S. E., Ossenkopf, V., et al. 2014, A&A, 571, A53
Beuther, H., Schilke, P., Menten, K. M., et al. 2002, ApJ, 566, 945
Beuther, H., Sridharan, T. K., & Saito, M. 2005, ApJ, 634, L185
Beuther, H. & Steinacker, J. 2007, ApJ, 656, L85
Chandrasekhar, S. & Fermi, E. 1953, ApJ, 118, 113
Chen, C.-Y., Ostriker, E. C., & Classy Team. 2015, in American Astronomical Society Meeting Abstracts, Vol. 225, American Astronomical Society Meeting Abstracts, 110.02
Draine, B. T. 2011, Physics of the Interstellar and Intergalactic Medium (Princeton Series in Astrophysics)
Fallscheer, C., Beuther, H., Zhang, Q., Keto, E., & Sridharan, T. K. 2009, A&A, 504, 127
Fernández-López, M., Arce, H. G., Looney, L., et al. 2014, ApJ, 790, L19
Fiege, J. D. & Pudritz, R. E. 2000a, MNRAS, 311, 85
Fiege, J. D. & Pudritz, R. E. 2000b, MNRAS, 311, 105
Galván-Madrid, R., Zhang, Q., Keto, E., et al. 2010, ApJ, 725, 17
Garay, G., Faúndez, S., Mardones, D., et al. 2004, ApJ, 610, 313
Hacar, A. & Tafalla, M. 2011, A&A, 533, A34
Hacar, A., Tafalla, M., Kauffmann, J., & Kovács, A. 2013, A&A, 554, A55
Heitsch, F. 2013a, ApJ, 769, 115
Heitsch, F. 2013b, ApJ, 776, 62
Henning, T., Linz, H., Krause, O., et al. 2010, A&A, 518, L95
Henshaw, J. D., Caselli, P., Fontani, F., Jiménez-Serra, I., & Tan, J. C. 2014, MNRAS, 440, 2860
Hill, T., André, P., Arzoumanian, D., et al. 2012, A&A, 548, L6
Inutsuka, S. & Miyama, S. M. 1992, ApJ, 388, 392
Jackson, J. M., Finn, S. C., Chambers, E. T., Rathborne, J. M., & Simon, R. 2010, ApJ, 719, L185
Johnstone, D., Fiege, J. D., Redman, R. O., Feldman, P. A., & Carey, S. J. 2003, ApJ, 588, L37
Kainulainen, J., Beuther, H., Banerjee, R., Federrath, C., & Henning, T. 2011, A&A, 530, A64+
Kainulainen, J., Hacar, A., Alves, J., et al. 2015, ArXiv e-prints
Kainulainen, J., Lada, C. J., Rathborne, J. M., & Alves, J. F. 2009, A&A, 497, 399
Kainulainen, J., Ragan, S. E., Henning, T., & Stutz, A. 2013, A&A, 557, A120
Kauffmann, J. & Pillai, T. 2010, ApJ, 723, L7
Kirk, H., Klassen, M., Pudritz, R., & Pillsworth, S. 2015, ApJ, 802, 75
Kirk, H., Myers, P. C., Bourke, T. L., et al. 2013, ApJ, 766, 115
Lee, K. I., Fernández-López, M., Storm, S., et al. 2014, ApJ, 797, 76
MacLaren, I., Richardson, K. M., & Wolfendale, A. W. 1988, ApJ, 333, 821
Men'shchikov, A., André, P., Didelon, P., et al. 2010, A&A, 518, L103+
Moeckel, N. & Burkert, A. 2015, ApJ, 807, 67
Myers, P. C. 2013, ApJ, 764, 140
Nagasawa, M. 1987, Progress of Theoretical Physics, 77, 635
Ossenkopf, V. & Henning, T. 1994, A&A, 291, 943
Ostriker, J. 1964, ApJ, 140, 1529
Peretto, N., Fuller, G. A., Duarte-Cabral, A., et al. 2013, A&A, 555, A112
Pineda, J. E., Rosolowsky, E. W., & Goodman, A. A. 2009, ApJ, 699, L134
Ragan, S., Henning, T., Krause, O., et al. 2012, A&A, 547, A49
Ragan, S. E., Henning, T., Tackenberg, J., et al. 2014, A&A, 568, A73
Schneider, N., Csengeri, T., Bontemps, S., et al. 2010, A&A, 520, A49
Smith, R. J., Glover, S. C. O., & Klessen, R. S. 2014, MNRAS, 445, 2900
Smith, R. J., Glover, S. C. O., Klessen, R. S., & Fuller, G. A. 2015, ArXiv e-prints
Smith, R. J., Longmore, S., & Bonnell, I. 2009, MNRAS, 400, 1775
Sridharan, T. K., Beuther, H., Schilke, P., Menten, K. M., & Wyrowski, F. 2002, ApJ, 566, 931
Tackenberg, J., Beuther, H., Henning, T., et al. 2014, A&A, 565, A101
Tackenberg, J., Beuther, H., Plume, R., et al. 2013, A&A, 550, A116
Tafalla, M. & Hacar, A. 2015, A&A, 574, A104
Wang, K., Zhang, Q., Testi, L., et al. 2014, MNRAS, 439, 3275
Zhang, Q., Wang, K., Lu, X., & Jiménez-Serra, I. 2015, ApJ, 804, 141
Zucker, C., Battersby, C., & Goodman, A. 2015, ArXiv e-prints